Simulated Sensitivity of Tropical Cyclone Size and Structure to the Atmospheric Temperature Profile

DIANA R. STOVERN[a] AND ELIZABETH A. RITCHIE[b]

Department of Atmospheric Sciences, The University of Arizona, Tucson, Arizona

(Manuscript received 6 July 2015, in final form 16 August 2016)

ABSTRACT

This study uses the WRF ARW to investigate how different atmospheric temperature environments impact the size and structure development of a simulated tropical cyclone (TC). In each simulation, the entire vertical virtual temperature profile is either warmed or cooled in 1°C increments from an initial specified state while the initial relative humidity profile and sea surface temperature are held constant. This alters the initial amount of convective available potential energy (CAPE), specific humidity, and air–sea temperature difference such that, when the simulated atmosphere is cooled (warmed), the initial specific humidity and CAPE decrease (increase), but the surface energy fluxes from the ocean increase (decrease).

It is found that the TCs that form in an initially cooler environment develop larger wind and precipitation fields with more active outer-core rainband formation. Consistent with previous studies, outer-core rainband formation is associated with high surface energy fluxes, which leads to increases in the outer-core wind field. A larger convective field develops despite initializing in a low CAPE environment, and the dynamics are linked to a wider field of surface radial inflow. As the TC matures and radial inflow expands, large imports of relative angular momentum in the boundary layer continue to drive expansion of the TC's overall size.

1. Introduction

During the period from August to October 2005, the United States endured several of the most expensive tropical cyclones (TCs) ever to occur in U.S. history. Hurricane Katrina accrued $108 billion in damages and caused an estimated 1200 fatalities in Louisiana and Mississippi (Blake et al. 2011; http://www.nhc.noaa.gov/dcmi.shtml). Hurricanes Wilma and Rita caused $21 and $12 billion, respectively, in damages. The devastation from these TCs was due to a combination of flooding, storm surge, and high winds (Beven et al. 2008). Although all three TCs reached category 5 on the Saffir–Simpson scale at some point in their lifetime (Saffir 1973; Simpson 1974), they were classified as considerably weaker category-3 hurricanes at landfall by the National Hurricane Center (Beven et al. 2008). However, all three of these devastating TCs had undergone a dramatic expansion in the size of their wind field after crossing the warm loop current west of 83°W in the warmer Gulf of Mexico (Fig. 1). While the maximum winds near the eyewalls of these intense TCs can produce devastating impacts, the true overall damage potential of a TC is associated with the total extent of damaging winds, which can also drive ocean waves and storm surge (Irish et al. 2008).

Tropical cyclones are historically known to range in size from a few tens of kilometers to up to 2000 kilometers in diameter (e.g., Holland and Merrill 1984; Chavas and Emanuel 2010). The size and associated wind field structure of a TC are important for predicting severity and duration of the TC once it makes landfall. Particularly for coastal communities, the size of the TC wind field can be catastrophic depending on the radius of hurricane-force winds and the duration of the event. In addition, predicting the size of the TC wind field is important to determine the potential impact of storm surge, the spatial scope of issued evacuation orders, and potential extent of wind damage (Brand 1972;

[a] Current affiliation: Cooperative Institute of Research for Environmental Sciences, University of Colorado Boulder, Boulder, Colorado.

[b] Current affiliation: School of Physical, Environmental, and Mathematical Sciences, University of New South Wales, Canberra, Australian Capital Territory, Australia.

Corresponding author address: Diana Stovern, Department of Atmospheric Sciences, The University of Arizona, Rm. 542, 1118 E. 4th St., Tucson, AZ 85721-0081.
E-mail: dstovern@atmo.arizona.edu

DOI: 10.1175/JAS-D-15-0186.1

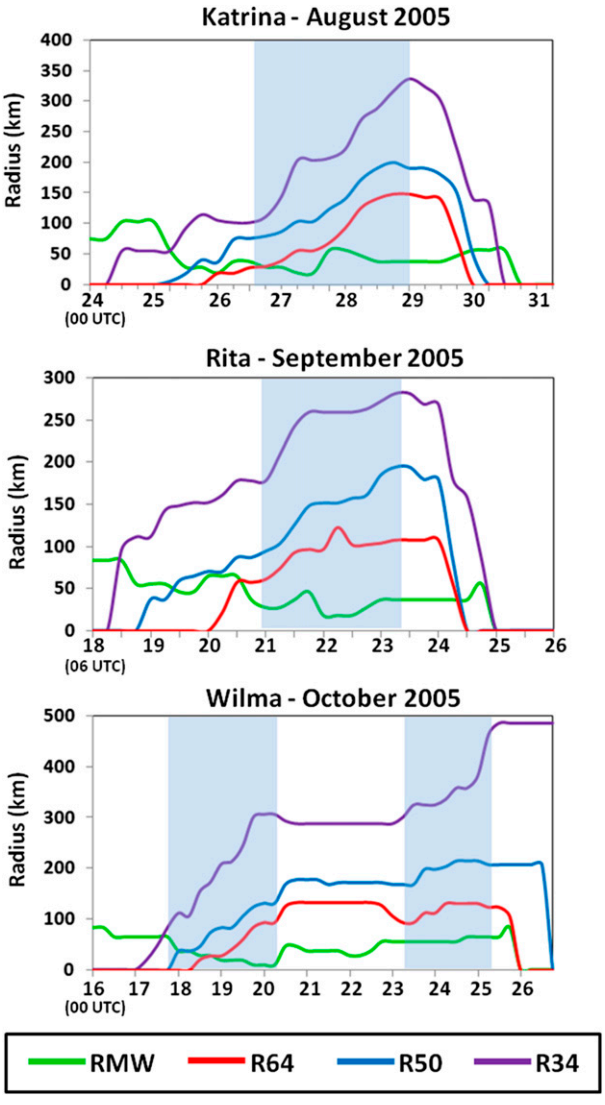

FIG. 1. The radius of maximum and 64-, 50-, and 34-kt winds for Hurricanes Katrina, Rita, and Wilma (2005) calculated from the Cooperative Institute for Research in the Atmosphere's (CIRA) best-track dataset (Demuth et al. 2006; http://rammb.cira.colostate.edu/research/tropical_cyclones/).

Weatherford and Gray 1988a,b; Kimball and Mulekar 2004; Knaff et al. 2014). During and subsequent to TC landfall, the structure of the precipitation field is important for predicting the severity of inland freshwater flooding, potential mudslides in complex terrain, and TC-spawned tornadoes from the highly convective outer rainbands. Hill and Lackmann (2009, hereafter HL09) suggest that these fields are, in part, dependent on the size of the storm. Thus, it becomes increasingly important that we understand the mechanisms that cause changes in the size and structure of a TC prior to landfall in vulnerable coastal regions.

There have been a number of studies investigating intensification, and particularly rapid intensification of TCs. In general, these have shown that intensity changes are only weakly correlated with size changes, and the dynamics controlling these parameters are fundamentally different (Weatherford and Gray 1988a; Merrill 1984; Maclay et al. 2008). While less research is available on factors that affect TC size and structure, there are several pertinent papers that explore how different environmental factors could cause size and structure changes within a TC, including angular momentum effects (e.g., Black and Anthes 1971; Challa and Pfeffer 1980; Holland 1983; Holland and Merrill 1984); environmental moisture and potential vorticity (e.g., May and Holland 1999; Wang 2009; HL09); moisture fluxes from the ocean (e.g., Xu and Wang 2010a,b, hereafter XW10a,b); environmental vertical wind shear (e.g., Frank and Ritchie 1999, 2001); and dry-air intrusion into the TC circulation (e.g., Kimball 2006).

HL09 show that the amount of midlevel environmental humidity can have a substantial impact on the intensity and spatial distribution of the outer-core precipitation field. HL09 hypothesized that more available moisture outside the TC core led to more latent heat release in the outer rainbands, resulting in higher production of diabatically generated potential vorticity. They proposed that band structure and lateral extent of precipitation are critical to the size of a TC wind field.

The amount of heat and moisture in the atmosphere available to a TC is intricately tied to the amount of surface energy fluxes from the ocean (Emanuel 1986). In addition to being a factor in intensification, high surface fluxes have also been found to be a factor in the size of the inner core of a TC (XW10a,b). XW10a found that removing the surface entropy fluxes outside the eyewall reduced both the radius of maximum winds (RMW) and radius of damaging winds (RDW) of the simulated TCs, and the decrease was inversely proportional to the radius outside of where the surface fluxes were removed. Removal of the surface entropy fluxes reduced the convective available potential energy (CAPE) outside the eyewall and suppressed the activity of spiral rainbands, which limited the size of the inner-core wind field in a manner similar to a process proposed in Wang (2009).

These studies contain important results that contribute to a small foundation of existing knowledge concerning TC size and structure changes. Perhaps more importantly, they provide motivation for further exploration into TC size changes. For example, most of these studies focus on changes to the inner-core wind field (RMW) and changes in core convection, but changes in the inner core are generally more linked to intensity changes and can often occur independently of outer-core and overall TC

size changes (Holland and Merrill 1984). Yet the studies specifically focused on structural changes associated with changing various environmental parameters in the numerical models, including moisture conditions, momentum fluxes, surface energy fluxes, vertical wind shear, and environmental flow. They demonstrated that TC size changes are clearly linked to environmental forcing but focused on how the environmental forcing affects inner-core changes, leaving an important gap in our knowledge concerning the physical processes behind TC size changes with respect to the entire wind field and not just the inner core.

This study addresses several gaps in the existing knowledge base on TC size and structure changes by examining how changes in the initial environmental temperature and specific humidity affect the outer-core wind structure and size of a TC. Particular focus is paid to structural evolution of the TCs in the different environments relative to a control simulation and how they are related to the changes in the surface energy fluxes, CAPE, and specific humidity. The evolution of the relative angular momentum (RAM) budget and potential vorticity (PV) field is also examined in order to identify the dynamic mechanisms leading to size change. The rest of this paper is structured in the following way: The mesoscale model and the diagnostics and analysis techniques are described in section 2. Section 3 presents the results of the structural differences between each simulation and explores the thermodynamic and dynamic aspects that separate a large-forming from a small-forming TC. Finally, discussion of the results and conclusions are provided in sections 4 and 5, respectively.

2. Methodology

a. Model description

The simulations in this study are performed using version 3.2 of the Advanced Research version of the Weather Research and Forecast (WRF) Model (ARW) developed at NCAR (Skamarock et al. 2005). The WRF Model is an atmosphere-only model that incorporates multiple nested grids and includes both explicit moist physical processes and a variety of cumulus parameterization and boundary layer schemes. The model has been adapted for use with idealized initial conditions to permit careful control of the initial-value experiments that enables us to examine the physical mechanisms associated with TC structural changes. WRF has been used by many previous sensitivity studies that explore mechanisms concerning TC size and intensity changes (e.g., Frank and Ritchie 2001; HL09; Fang and Zhang 2012; Mallard et al. 2013).

The model is configured with 33 vertical levels, 8 of which are located below 850 hPa, and the topmost level is specified at 50 hPa. The parent domain (D1) is square, with a size of 7506 km in each direction and a horizontal grid spacing of 27 km, ensuring that large-scale circulation features are well specified and that the boundaries are far from the region of interest in the interior of the domain. There are also two two-way nested inner-square domains of spatial sizes 2052 km (D2) and 720 km (D3) with grid spacing of 9- and 3-km resolution, respectively. D3 is capable of resolving moist processes within the eye and eyewall region, while both inner and outer rainbands are well resolved by D2 (e.g., Frank and Ritchie 2001; Ritchie and Frank 2007; Ritchie and Elsberry 2007; XW10a). D2 is initialized in the center of D1, which is large enough to ensure that D2 can move freely through the simulation without experiencing any boundary interactions with D1. D3 is centered within D2 such that the TC vortex is approximately centered within D3 at 15°N, 135°W. Both D2 and D3 are vortex-following nests, which makes it convenient to study how the surrounding environment affects the inner-core dynamics while automatically tracking the TC.

The boundary layer is parameterized using the Mellor–Yamada–Janjic (MYJ) scheme (Janjic 1990, 2002). The MYJ works in conjunction with the Eta similarity scheme, which is used to parameterize the surface layer and calculate surface energy fluxes. The lower boundary in our model is an ocean surface with a specified SST that remains constant throughout the integration of each simulation. Holding the SST constant, while artificial, enables us to more readily isolate individual environmental factors associated with TC size and structure change.

The outer two domains employ the Kain–Fritsch cumulus parameterization scheme (Kain and Fritsch 1993) to represent unresolved convection. Explicitly resolved convection is applied on all domains using the WRF single-moment 6-class scheme, which employs ice, snow, and graupel processes (Hong and Lim 2006). The application of this parameterization on the innermost domain is important for resolving the finer features in the core precipitation and rainbands of the TC; however, it has little effect on the two outer domains. Radiation processes are handled via a Rapid Radiative Transfer Model for longwave radiation (Mlawer et al. 1997) and the Dudhia scheme for shortwave radiation (Dudhia 1989). To simplify the interpretation of the results, land effects are removed by employing a ''water world.'' Using the above configuration, a total of seven idealized simulations are run and analyzed for this study. Each simulation is integrated for 5 days, and the output is saved every 3h. The control simulation is also run out

for a further 120 h to ensure that steady-state conditions have been reached. The analysis is performed by comparing the sensitivity simulations to the control simulation. This allows for a comparison of the impact of the changes made to the control profile similar to an analysis that examines the impact on a base forecast track by changing factors in the forecast model.

b. Experimental design

The control environment is modeled after the experiments of Frank and Ritchie (1999) and is initialized with no horizontal or vertical winds and with clear-sky conditions on an f plane (constant Coriolis at 15°N). The mass field and lateral boundary conditions are derived by using the virtual temperature and humidity values from the McBride and Zehr (1981) prestorm composite data. The surface boundary condition is supplied by specifying a constant SST of 302 K (28.84°C) everywhere in the domain.

The radial size and structure of the initial TC wind field is specified by (Chan and Williams 1987):

$$v_\lambda = V_m \frac{r}{r_m} \exp\left\{\frac{1}{b}\left[1 - \left(\frac{r}{r_m}\right)^b\right]\right\}, \quad (1)$$

where v_λ is the tangential wind, V_m is the maximum wind, r is the radial distance from the center of the TC, r_m is the radius of maximum winds, and $b = 1$ is a parameter that sets the overall size of the initial wind field at 260 km for the radius of 34-knot (kt; 1 kt = 0.51 m s^{-1}) winds (R34). The TC cyclonic wind varies in the vertical as

$$V = \frac{[V_m \times 3.0(\sigma/0.9)]}{[2.0 + (\sigma/0.9)^3]}, \quad (2)$$

where σ is the normalized vertical coordinate $(p - p_T)/(p_s - p_T)$, p_s is the surface pressure, and p_T = 50 hPa is the pressure specified at the top of the model. Using Eqs. (1) and (2), a three-dimensional wind field is calculated in cylindrical coordinates. Next, the mass fields are calculated using the hypsometric and thermal wind relations, and a Gaussian moisture anomaly is added to the center of the vortex to facilitate onset of convection in the TC core. Finally, the variables are remapped to a Cartesian coordinate system and combined with the environmental fields. The result is a weak, hurricane-strength vortex in gradient balance with the mass field at 15°N, with maximum winds of 65 kt located 100 km from the center of the TC.

To create the different atmospheric environments for the sensitivity simulations, a basic alteration to the control environment is undertaken. The entire vertical profile of virtual temperature is modified by a constant amount of ± 1, ± 2, and ± 3 K without altering the SST and applied to the entire atmospheric computational domain (Fig. 2). The simulations warmer than the control are referred to as W1, W2, and W3, and those cooler than the control are C1, C2, and C3. Because the initial relative humidity profile is held constant, the modifications to the temperature profile correspond to a change in the specific humidity profiles (Fig. 3a). The initial amount of CAPE also changes so that the coolest simulation, C3, initializes with an environmental CAPE of 168 J kg^{-1}, while the warmest simulation, W3, initializes with a CAPE value of 1350 J kg^{-1}. The initial atmospheric static stability (Fig. 3b) and environmental lapse rate are essentially unchanged by these changes in the virtual temperature profile but immediately begin changing once the model starts running.

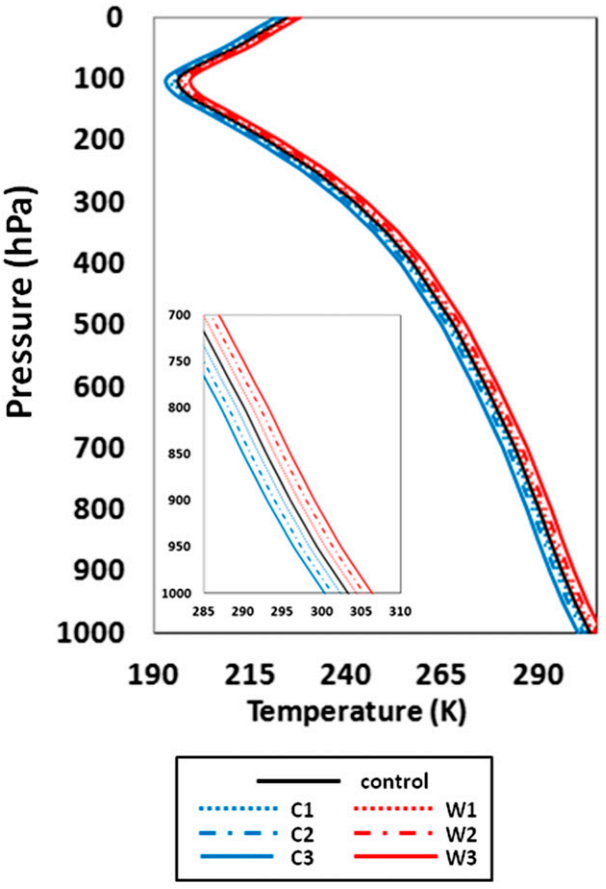

FIG. 2. Initial environmental virtual temperature profiles applied to the seven simulations. Blue (red) lines indicate profiles that are 1–3 K cooler (warmer) than the control profile. The inset image shows zoomed-in profiles up to 700 hPa.

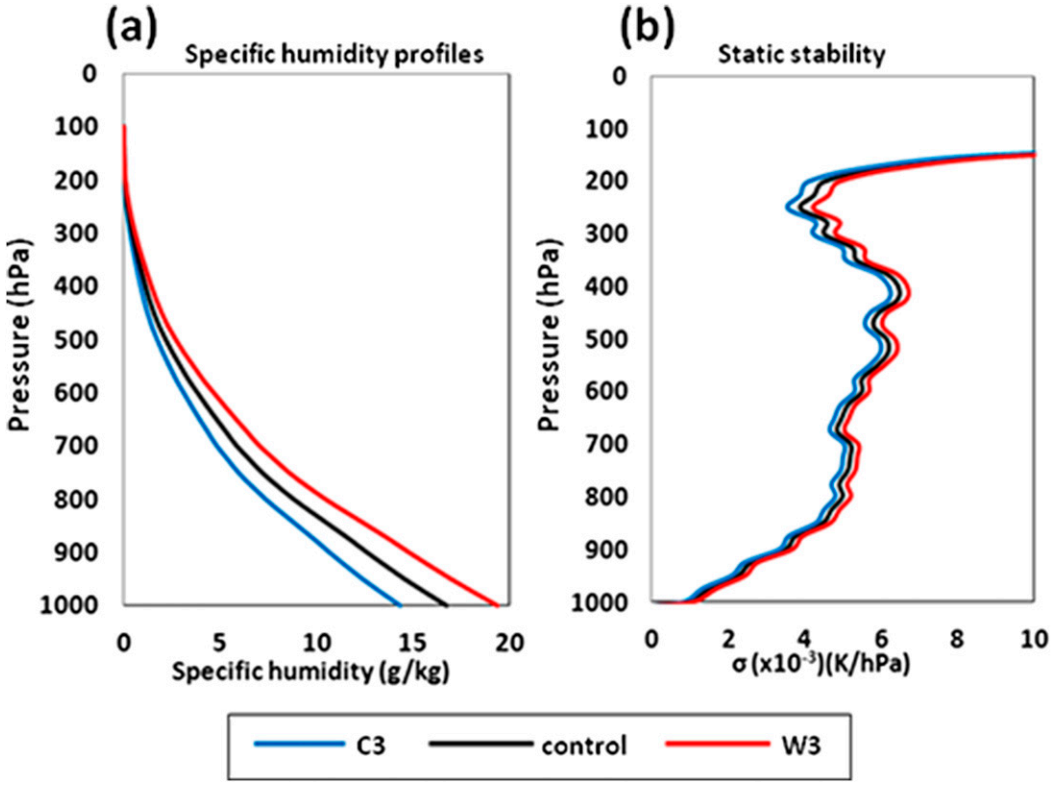

FIG. 3. Initial vertical profiles for the control, C3, and W3 simulations: of (a) specific humidity (g kg^{-1}) and (b) static stability ($\times 10^{-3}$ K hPa^{-1}).

As a final consequence of changing the atmospheric temperature profile, the temperature and vapor pressure difference between the ocean and surface air layer produce almost immediate changes to the surface fluxes. The latent heat (LH) and sensible heat (SH) fluxes are controlled by three variables: the difference in temperature between the ocean and surface air ($T_{\text{ocean}} - T_{\text{surface\_air}}$); the difference in vapor pressure between the ocean and surface air [$e_{(\text{ocean}\_T)} - e_{(\text{air}\_T)}$]; and the wind speed (Malkus and Riehl 1960). These physical processes are parameterized in the model through a boundary layer scheme (Janjic 1994), which also includes a viscous sublayer and accounts for sea roughness through the Reynolds number.

Table 1 shows the temperature difference between the sea surface temperature and the air temperature of the lowest level of the atmosphere after the changes to the virtual temperature profile are applied. Also included are the resulting vapor pressure differences. The surface flux calculations in the model are dependent on surface wind speed in addition to the air–sea temperature and vapor pressure difference. Since each simulation begins with the same strength TC, the fluxes are initially driven by the air–sea temperature difference so that a warmer (cooler) atmosphere leads to lower (higher) surface LH and SH fluxes as long as the same underlying SST is maintained.

Note that some of these initial conditions are not realistic. The intent of this study is to understand the physical mechanisms that can lead to changing wind field structures in TCs. Thus, the methodology behind this set of simulations—to systematically alter the environment—makes it possible for us to better isolate cause and effect within these simulations. However, because each of the different physical characteristics of the environment may potentially have an impact on TC development, all must be considered when interpreting

TABLE 1. Initial differences in temperature (°C) and vapor pressure (hPa) between the sea surface and lowest level of atmosphere for the initial set of seven simulations. The SST is 302 K in each simulation.

Case	T(SST) − T(air) (°C)	e(surf) − e(air) (hPa)
C3	3.6	17.0
C2	2.8	15.7
C1	1.9	14.4
Control	1.1	13.1
W1	0.3	11.7
W2	−0.6	10.3
W3	−1.4	8.8

the results. Because of this, the analysis of the simulations will be undertaken by examining differences in TC structural evolution from the control simulation.

Operational forecasters at the National Hurricane Center (NHC) routinely estimate size in terms of the radii of 34–50- and 64-kt surface winds and radius of maximum winds. There is no standard metric that defines the size of the convective field, but some observational studies have described it in terms of the eyewall region, the inner-rainband region, and outer-rainband region (e.g., Cecil et al. 2002; Molinari et al. 1999). Most studies find that the size of the wind field is intricately tied to the structure of the convective field (e.g., HL09; XW10a,b), so our analysis method has to consider the structural regions of both fields while still maintaining consistency with operational standards. To do this, we use the RMW to quantify the size of the inner core, the radius of 64-kt (R64) and 50-kt (R50) winds to describe the size of the outer-core, and the radius of 34-kt winds is used to delineate where environmental interactions can occur to produce overall size changes in the TC (Merrill 1984; Kimball 2006; HL09). We will also often refer to the ''regions'' of the inner core, outer core, and interactive envelope in order to encapsulate the impact of different environmental variables on the structure of both the wind and precipitation fields. These regions are approximately defined in the following manner: the inner-core region contains the RMW, convective eyewall, and inner spiral rainbands; the outer-core region roughly contains the R64, R50, and any outer spiral rainbands that form; and the region describing the overall size starts at the edge of the outer-core region and extends to the R34. All size parameters are azimuthally averaged using the 10-m wind speeds. Primary focus is paid to the processes that link changes in the environment to changes in the R64, R34, and the associated convective structure. Most of the diagnostics are azimuthally averaged quantities calculated at 5-km increments from the center of the TC. This includes anything that is displayed as a function of radius. Variables shown that are not explicitly calculated by WRF include the potential vorticity, CAPE, angular momentum fluxes, and radial and tangential wind fields.

3. Simulation results

a. Intensity and wind structure

Each simulation is initialized with the same central pressure and wind structure (Fig. 4a). Thereafter, all simulations except for C2 and C3 evolve similarly to the control, reaching a maximum intensity around 48–60 h and then slightly weakening through the end of the 120-h period. The tropical cyclones in the warm environments (i.e., W1, W2, and W3) end with final intensities slightly higher than the control. The C2 and C3 simulations have slightly reduced intensification rates after approximately 12 h but generally strengthen through the simulation period and reach their final intensities at 120 h. C2 slightly differs from C3 in that it weakens between 48 and 72 h before intensifying again to become the most intense tropical cyclone in the set.

The RMW evolves with some correspondence to the intensification rate (Fig. 4b). After the initial spinup period, the slower-intensifying C2 and C3 TCs maintain the largest RMWs through the majority of their simulation, but C2 contracts after 84 h while reintensifying. In contrast, the warm-atmosphere TCs evolve with a smaller RMW during the period when their intensification rate is higher than C2 and C3 (i.e., 24–60 h). The TCs continue to maintain a smaller RMW than the TCs in the cooler atmospheres through 120 h, but their RMW slightly expands while they weaken.

The outer-core wind field, represented by the R64, develops at approximately 12 h and steadily increases for all TCs (Fig. 4c). However, progressively larger storms evolve when the initial environmental temperature profile decreases from W3 to C3. The outer-core evolution in C3 is particularly interesting after about 84 h, when the rate of expansion rapidly increases. Between 12 and 120 h, the R64 in C3 increases by 160 km compared to 51 and 49 km in the control and W3, respectively.

The largest differences occur in the R34, which is not particularly sensitive to temperature changes within the first 60 h but divides into three groups thereafter (Fig. 4d). The C2 and C3 TCs make the largest expansion, increasing in size by 167 and 348 km, respectively, during the final 60 h. The C1 and control TCs make a comparatively smaller expansion during this period, increasing by 56 and 40 km, respectively. The remaining TCs (i.e., W1, W2, and W3) slightly contract in size.

It is clear that, based on whether the initial environments are warmed or cooled relative to the control, the associated atmospheric conditions develop such that cooling leads to a TC that increases in size while warming leads to a TC that decreases in size. When the initial atmospheric temperature is modified by 1°–2°C, the differences in the structural development compared to the control are somewhat subtle, so the rest of this paper will focus on the extreme cases in the set, C3 and W3, which allows us to more easily identify the mechanisms that separate large-forming TCs from those that contract.

b. Precipitation structure

Radar reflectivity (Fig. 5) and azimuthally averaged, 3-h precipitation tendencies, which quantify the intensity

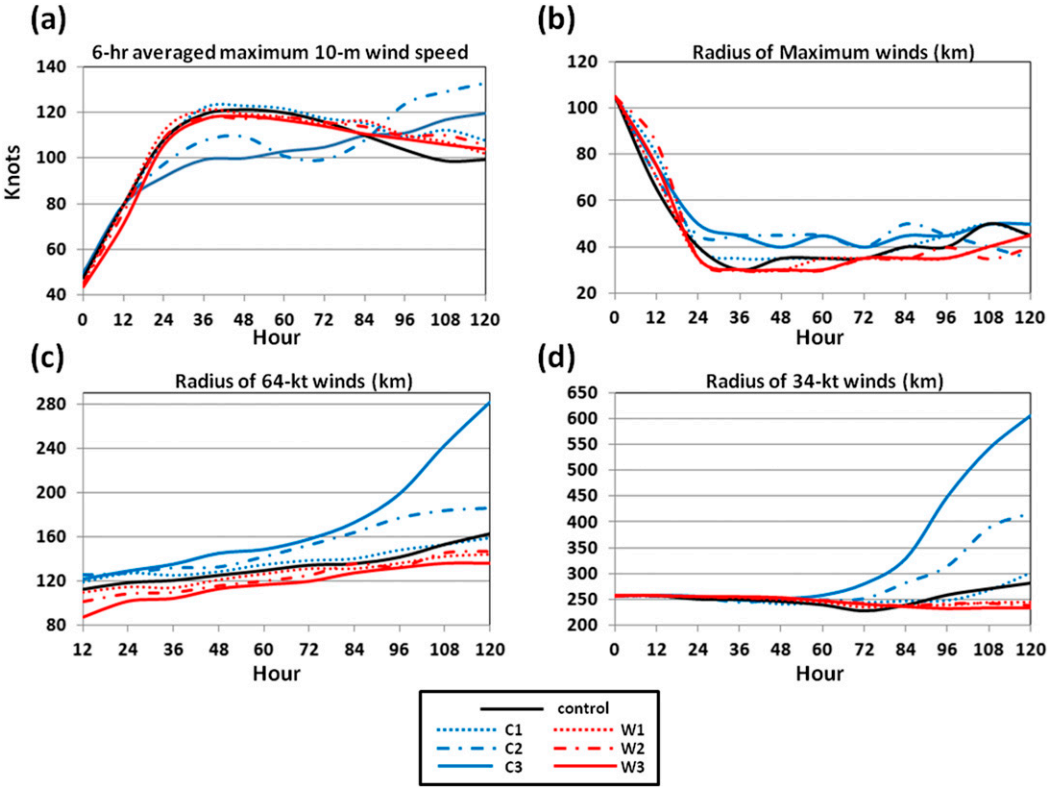

FIG. 4. Time evolution for all seven simulations of: (a) maximum 10-m wind speed (kt), smoothed with a centered 12-h running mean; (b) RMW (km); (c) R64 (km); and (d) R34 (km). The size parameters are measured using azimuthally averaged values from the 10-m wind field.

and size of the precipitation field (Fig. 6), are used to identify structural differences in the precipitation between the simulations. At 24 h, W3 and the control have a similar structure of an intense, inner core of precipitation surrounding a complete eyewall with a weak outer rainband between 100 and 150 km from the center (Figs. 5a,b). Figure 6a shows that the highest inner-core precipitation rates are located near the RMW, but the radial extent of the inner-core precipitation field stays confined within 100 km of the center. In contrast, C3 develops with a weaker and much more disorganized core of convection but attains an overall larger precipitation field with multiple rainbands, resulting in a broader area of precipitation (Figs. 5c, 6a). Through 60 h, W3 and the control become more annular, and the inner-core convection strengthens (Figs. 5d,e, 6b). The maximum precipitation rates in C3 are half the magnitude of the control and W3 at this point, but the overall size of the precipitation field is larger. C3's inner core also extends slightly beyond 100 km with an outer rainband located approximately at a 175-km radius. The inner-core convection in the control and W3 weaken through the final 60 h of the integration, although the control does develop strong outer-core rainbands by 120 h (Figs. 5g,h, 6c). In contrast to W3, both the inner-core and outer-core convection strengthen in C3 through the remainder of the simulation (Figs. 5f,i). By 120 h, C3 has multiple outer-core rainbands and a total convective field that extends to a radius at least 250 km from the TC center (Fig. 6c). Interestingly, C3's inner-core precipitation rates at 120 h never reach the magnitude that W3 and the control reach at 60 h, despite the TCs having similar intensities at these times.

These results suggest that larger-forming TCs are associated with increased outer-core rainband formation, which is favored when the atmospheric temperature is initially cooled while the SST remains unchanged. The results are consistent with those of Wang (2009), HL09, XW10a, and XW10b. Wang (2009) found that outer-core rainbands increase diabatic heating outside the RMW and cause net warming, which reduces the pressure gradient across the inner core and expands the RMW while also decreasing the maximum wind speed. Outer rainbands can also reduce the radial inflow to the inner core, effectively reducing inward transport of boundary layer mass and moisture to cause weakening in the vortex intensity (Fudeyasu and Wang 2011; Didlake and Houze 2013). This mechanism explains why

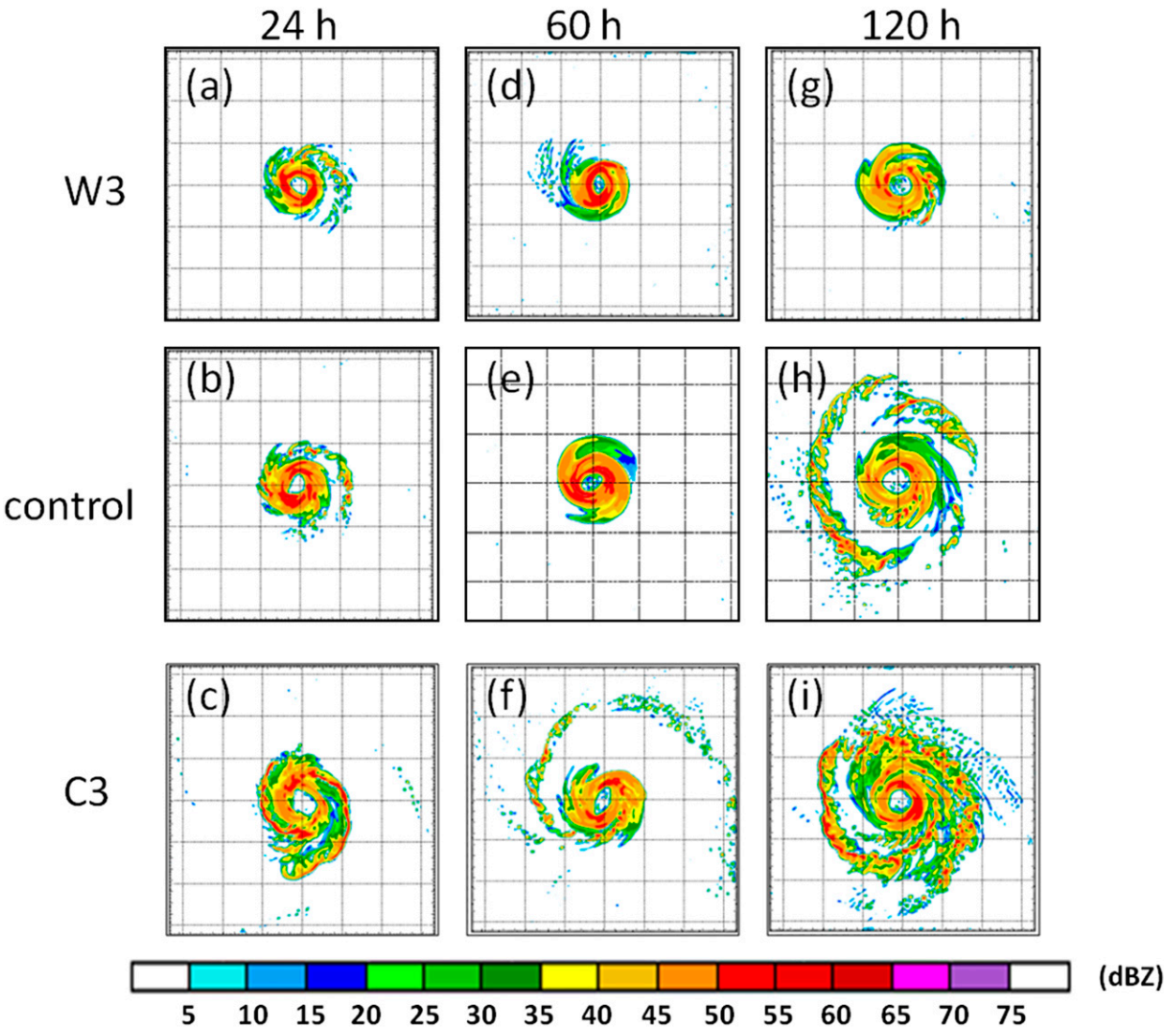

FIG. 5. Composite radar reflectivity (dBZ) at 24, 60, and 120 h for the W3, control, and C3 simulations. Gridlines are 1° × 1°.

C3 has a reduced intensification rate and a larger RMW throughout the majority of its simulation. Since outer-core rainband formation seems to be integral to size increases (e.g., HL09), the next two sections will explore differences between the C3 and W3 simulations that might lead to rainband formation in the former and not in the latter.

c. *Role of surface fluxes and CAPE*

Figure 7 shows the temporal evolution of SH and LH fluxes averaged within 0–100, 100–250, and 250–600 km from the center. These radii correspond to the regions that best capture inner-core, outer-core, and interactive envelope regions. The interactive envelop region is where the TC begins to interact with the environment to produce overall size (R34) changes. All regions of each TC display a strong sensitivity to the initial imposed air–sea temperature and vapor pressure difference. In general, the surface fluxes are highest in C3 and decrease with each incremental increase in atmospheric temperature. Since the fluxes in Figs. 7a and 7b are calculated within a 100-km annulus from the TC center, where the surface winds are strongest, their evolution is more variable and increasingly dependent on the intensifying inner-core wind field.

In the outer core, where the winds are weaker, the flux values are less dependent on the growing wind field, particularly prior to 72 h (Figs. 7c,d). Notice in Fig. 7c how the initially negative air–sea temperature difference in W3 impacts the outer-core SH fluxes in the first 9 h, which start slightly negative but become positive as evaporative cooling in the developing convective field

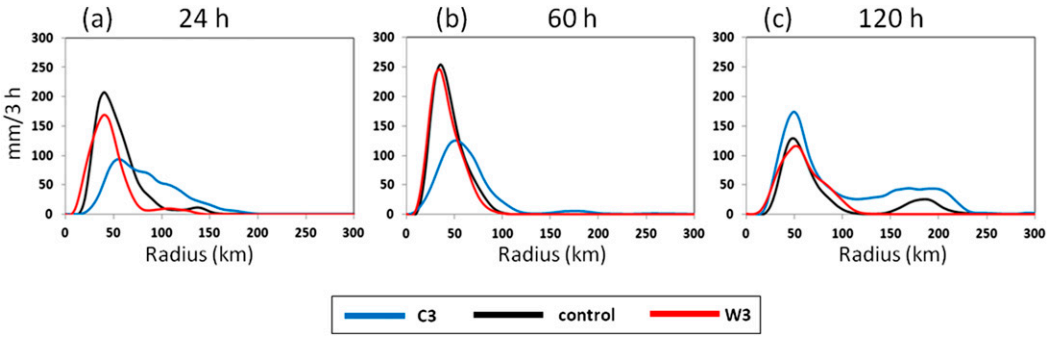

FIG. 6. Azimuthally averaged 3-h precipitation tendencies (mm) for the C3, control, and W3 simulations: (a) 24, (b) 60, and (c) 120 h.

rapidly cools the boundary layer. After 72 h, the expansion of the wind field becomes evident in C3 and to some extent the control, demonstrated by the increasing outer-core fluxes. In the environment, the fluxes are small and remain steady or slightly increasing during the 120-h period (Figs. 7e,f).

The amounts and radial distributions of LH and SH fluxes are known to impact the inner-core size and intensification of a TC by impacting the radial distribution of atmospheric CAPE, which favors the development of outer-core rainbands (e.g., XW10a). Our results demonstrate that the high surface fluxes in C3 help to either maintain or increase CAPE in the convective regions of the TC (Figs. 8a,b) and the environment (Fig. 8c), facilitating inner- and outer-core rainband development. Interestingly, the CAPE in W3's convective region is slightly higher than in C3 through 36 h, but it does not result in more active outer-core rainband formation. This suggests that an additional *or stronger* mechanism is present in C3 that is enhancing early development of rainbands beyond the eyewall.

The higher inner-core CAPE (Fig. 8a) and moisture in the control and W3 during the first 48 h of the simulation likely helped to produce the higher inner-core precipitation rates (Figs. 6a,b), stronger eyewall convection (Figs. 5a,b,d,e), and higher intensification rates (Fig. 4a). Yet, despite sufficient CAPE being maintained in both the inner and outer cores thereafter, W3 and the control still weaken, and W3 never displays any significant outer-rainband development. In addition, the amount of inner-core CAPE appears to have little correspondence with the maximum attained intensity in these simulations, which is consistent with the findings of Persing and Montgomery (2005), who found that CAPE is not a factor in determining a TC's maximum potential intensity. The primary result here is that, because outer-core rainband formation is dampened in W3 despite the presence of sufficient CAPE, there must be a dynamic mechanism that is either absent or significantly weaker in this region compared to C3.

d. Radial wind field and convective structure

The initiation of convection in each TC is intricately tied to the strength and structure of the developing radial inflow in the boundary layer. As early as 2 h into the simulation, the developing radial wind field in C3 is already stronger than in W3 and expands farther from the TC center (Figs. 9a,b). The strengthening radial inflow in C3 leads to stronger vertical velocities (VV) by 4 h (Figs. 9c,d) that by 7 h exhibit a double-maxima structure (Fig. 9e). The two VV maxima are associated with the inner- and outer-core rainbands observed in the reflectivity in Fig. 5c. In contrast, W3 develops with a single-maximum VV structure (Fig. 9f) that, by 21 h, is stronger than both of C3's VV maxima (Figs. 9g,h), consistent with a more intense TC (e.g., Fig. 4a). The double-maxima VV structure in C3 is associated with a double-maxima radial wind field structure in the boundary layer (Figs. 9e,g). Converging radial inflow immediately radially inward of the secondary wind maxima in Figs. 9e and 9g is likely forcing the secondary VV maxima in the same location, about 125 km from the TC center.

Since the initial wind field is nearly identical between the simulations, the mechanism to develop such different radial wind structures in the boundary layer likely results from the differences in the surface energy fluxes. In the WISHE theory, TC development is driven by an instability that relies on a feedback between radial temperature gradients that drive the circulation and radial gradients of sea–air heat transfer associated with gradients of surface wind speed (Emanuel 1986). A similar mechanism could explain the differences seen here, where the high surface SH fluxes in C3 create a favorable radial temperature gradient in the boundary layer for the expansion of the tangential and radial wind fields. Note that the initial 950-hPa temperature change

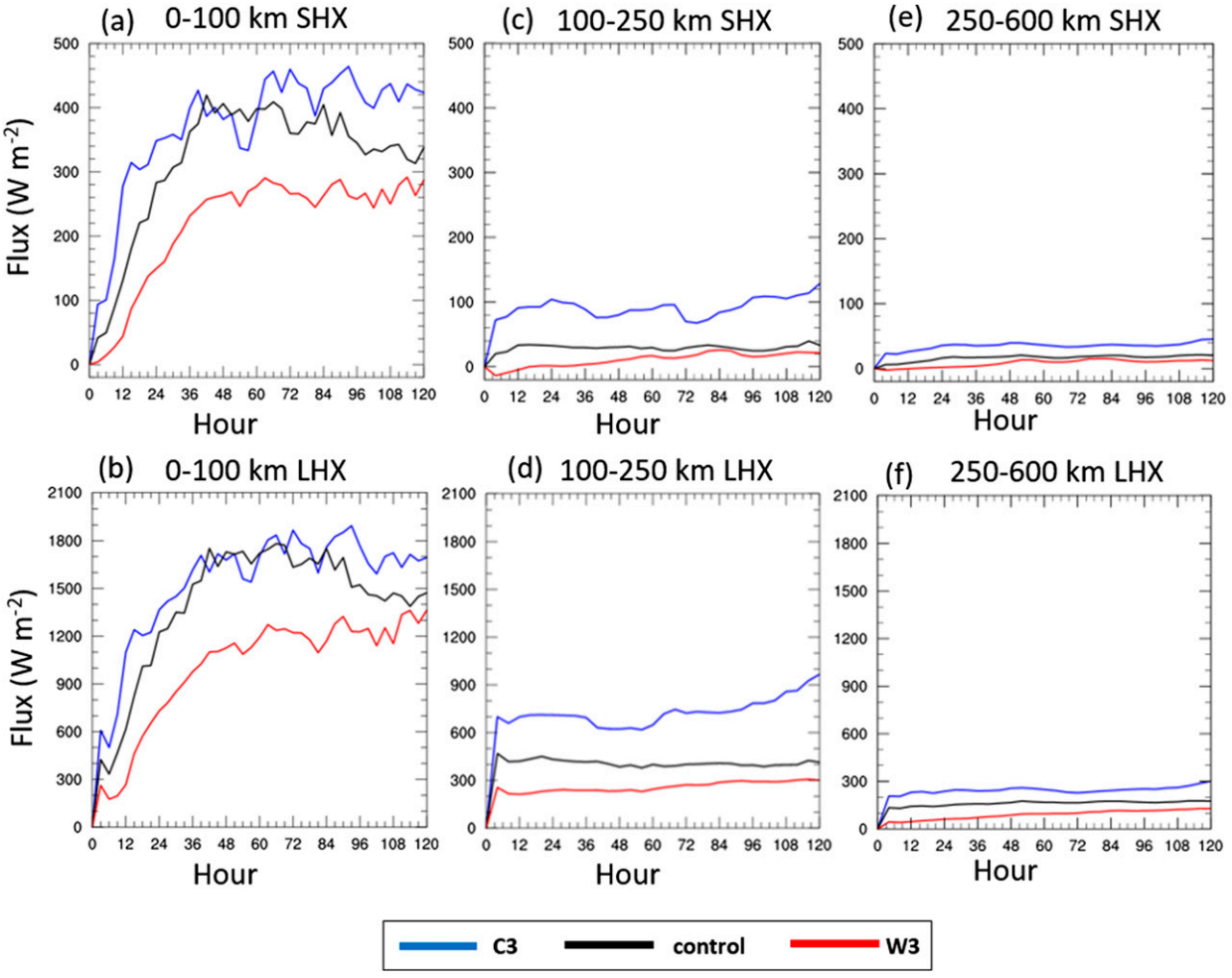

FIG. 7. Temporal evolution of the (top) sensible and (bottom) latent heat flux (W m^{-2}) averaged within (a),(b) 0–100 km (inner core); (c),(d) 100–250 km (outer core); and (e),(f) 250–600 km (interactive envelope region) from the TC center.

with radius is nearly identical in Fig. 10a. After the simulation starts, the positive SH fluxes in C3 produce a surface temperature maximum at the RMW and a negative-radial temperature gradient just outside the RMW (Fig. 10b). A similar process was also noted in Ma et al. (2015). In contrast, the negative SH fluxes in W3 produce a temperature minimum near the RMW and a strong, positive-radial temperature gradient beyond 100 km that may be constraining the radial inflow in the boundary layer. By 4 h, W3 has developed considerable structure in the surface temperature field with a weak, negative gradient from 50 to 125 km that becomes strongly positive from 125 to 200 km (Fig. 10c). The resulting radial inflow is weak, shallow, and confined within 200 km of the center of the TC (Fig. 9d). Beyond 4 h, the strengthening convection enhances boundary layer radial inflow in all TCs, and expansion of the radial wind field is less dependent on radial temperature gradients and becomes more dependent on the cooperative interaction between the surface energy fluxes and the expanding tangential wind and precipitation fields.

e. *PV and RAM associated with the wind field expansion*

Figure 11 shows time–radius Hovmöller diagrams of azimuthally averaged PV diagnostics associated with the precipitation field. Composite reflectivity is shaded in Figs. 11a and 11b as a proxy for the extent of convection in the eyewall and rainbands. The PV tendency and the R64, R50, and R34 are overlaid in order to determine if our results are consistent with those of HL09, who found that diabatic PV production within the outer rainbands broadens the PV distribution, which results in an expansion of the TC outer-core wind field.

Similar to HL09, our results show that the production of PV is generally cellular in nature, in accordance with

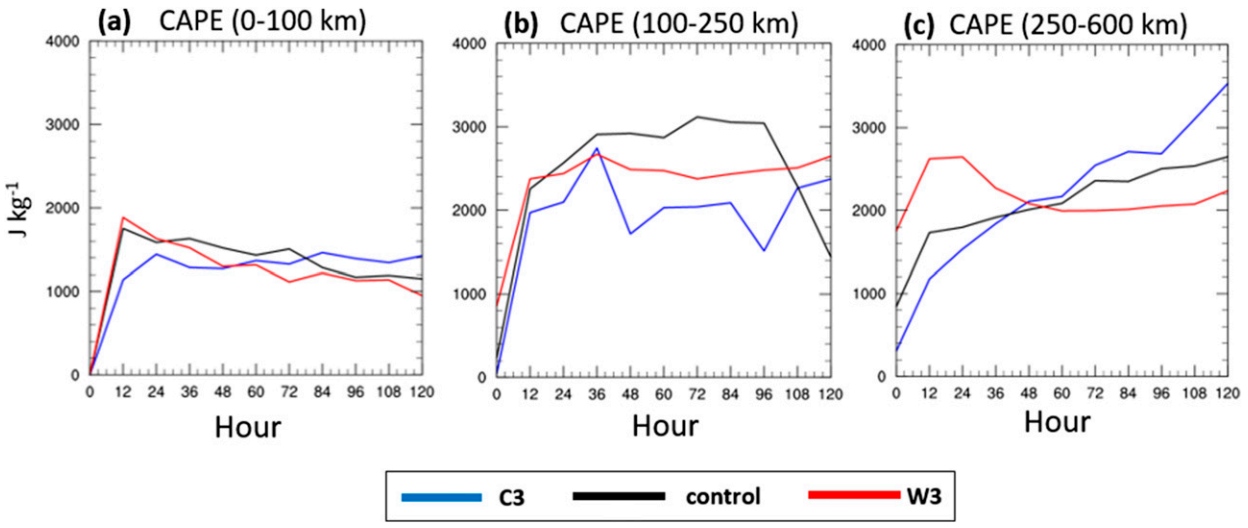

FIG. 8. Temporal evolution of CAPE (J kg^{-1}) averaged within (a) 0–100 km (inner core); (b) 100–250 km (outer core); and (c) 250–600 km (interactive envelope region) from the TC center.

the convective structure of spiral rainbands. Thus, the azimuthal averaging in Fig. 11 smooths and weakens the PV field, especially in the outer rainbands. Nevertheless, it can be seen that, by 24 h, the region of diabatic PV generation extends radially out to about 150 km in C3 (Fig. 11a), which is nearly twice that of W3 (Fig. 11b). The region of diabatic forcing and PV generation continues to expand in C3 so that, by 96 h, it extends to about 250 km. In contrast, the PV generation expands only slightly in W3 and generally stays confined within 100 km, corresponding to slight growth in the R64 and R50. This appears to be consistent with the findings of HL09 that there is a correlation between PV generation in the outer rainbands and outer-core size change. Yet, despite the continual growth of W3's R64 and R50, the R34 actually contracts, suggesting that a dynamic component is missing in W3's interactive envelope region that is required for overall size increases.

XW10b found that increased production of diabatic potential vorticity outside of the eyewall enhances the radial advection of absolute angular momentum (AAM) via the vertical absolute vorticity term $\overline{u}\,\overline{\zeta_a}$ in the angular momentum budget, where $\overline{\zeta}_a = \overline{f} + /\partial(R\overline{V_T})/R\partial R$. The 850-hPa PV overlaid with the radial wind velocities in Figs. 11c and 11d shows that the radial inflow and PV field in the outer-core region are much stronger in C3, likely increasing $\overline{u}\,\overline{\zeta_a}$ to facilitate an expanding wind field. Interestingly, ''pulses'' of enhanced radial inflow outside of the RMW in C3 (Fig. 11c) seem to correspond with bursts of outer-core convection in Fig. 11a. This can also be seen to some extent in W3 (Figs. 11b,d), although the radial inflow is constricted to much smaller radii.

The role of the outer rainbands on the size changes in C3 and W3 are further assessed through an analysis of the AAM budget. This study draws on the methodologies from Tuleya and Kurihura (1975), McBride (1981), Chan and Chan (2014), and Li et al. (2015) for the calculations. The azimuthal mean, local tendency of AAM expressed in cylindrical coordinates is defined as

$$\frac{dm}{dt} = -\nabla \cdot V_m - f V_R R + R F_T. \tag{3}$$

The first term on the right-hand side represents the horizontal transport, which, when divided into the mean and eddy components, is expressed as $\overline{V_T}\,\overline{V_R}$ and $\overline{V_T'}\,\overline{V_R'}$, respectively. The overbar represents the azimuthal mean, the prime is the deviation from the azimuthal mean, and the tangential and radial wind velocities are represented by V_T and V_R. The horizontal convergence of the mean RAM flux is proportional to $-\overline{V_T}\,\overline{V_R}$ on the perimeter of the circle (McBride 1981). The third term on the right-hand side is the symmetric Coriolis torque, where f is the Coriolis factor, and radius is denoted by R. The last term arises from friction, approximated by

$$F_T = \rho C_D V_S^2, \tag{4}$$

where $C_D = (0.75 + 0.67|V_S|) \times 10^{-3}$, V_S is the surface tangential wind velocity, and ρ is surface air density. Vertical advection of AAM is not included in the analysis, because the contribution has been found to be nearly negligible beyond an 80-km radius (Li et al. 2015; Chan and Chan 2014; Merrill 1984), which is outside the region of interest in this study. Our calculations for C3 and W3 show that the horizontal convergence of mean

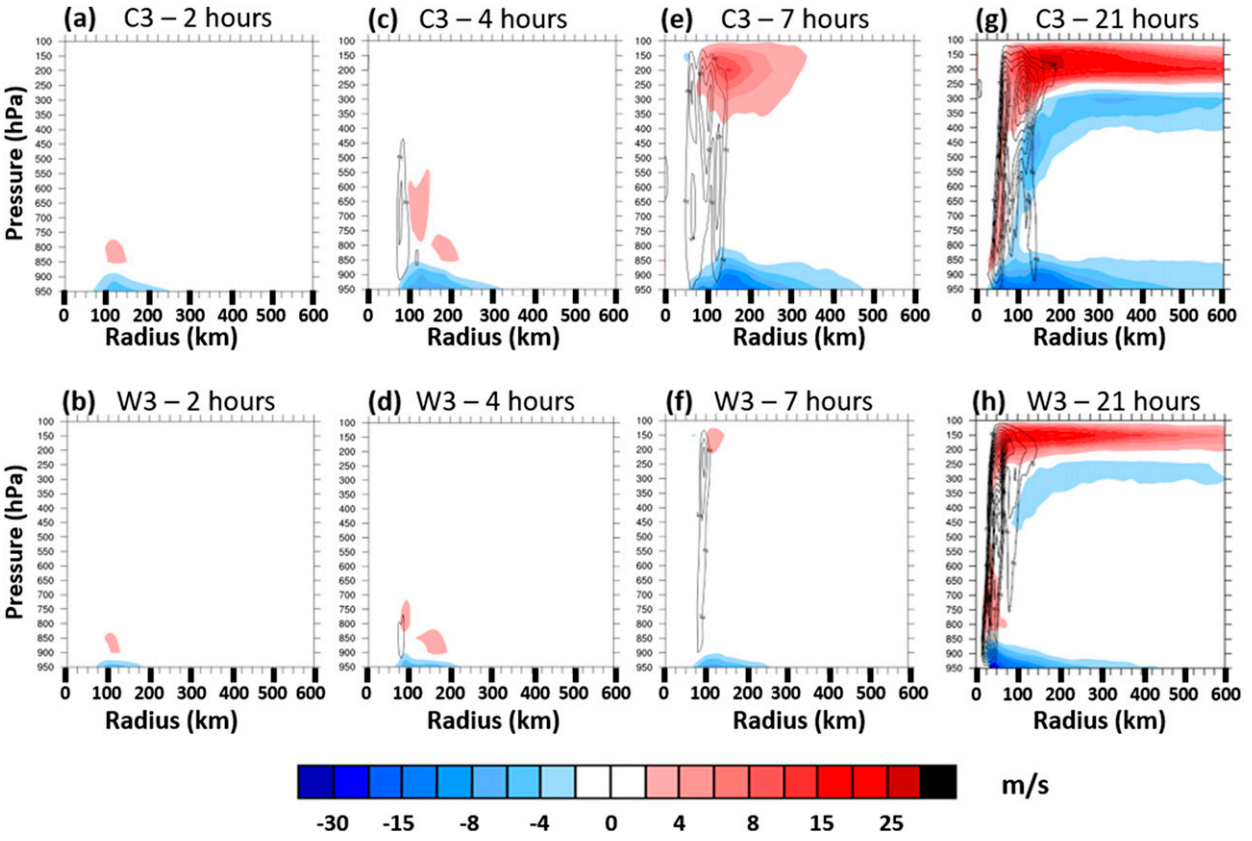

FIG. 9. Azimuthally averaged vertical wind velocities (contours with increment = 0.2 m s^{-1}) and radial-wind circulation (color shaded, m s^{-1}) for (top) C3 and (bottom) W3 at (a),(b) 2; (c),(d) 4; (e),(f) 7; and (g),(h) 21 h.

RAM flux and frictional dissipation are the dominant contributors to the AAM tendency. The Coriolis torque makes a small contribution at large radii, particularly in C3, and the eddy fluxes are near zero beyond a 100-km radius. These results are generally consistent with other studies that have assessed the angular momentum budget for idealized simulations (e.g., Sawada and Iwasaki 2010; Chan and Chan 2014).

Vertical cross sections of the mean RAM flux convergence show where positive gains are being made to the AAM tendency. At 24 h, convergence of RAM is higher in the boundary layer beyond the RMW in C3 (Fig. 12a) compared to W3 (Fig. 12b). Li et al. (2015) observe similar characteristics in their simulations and attribute changes in the R50 to increased convection outside of the RMW, or rapid filamentation zone, which enhances the secondary

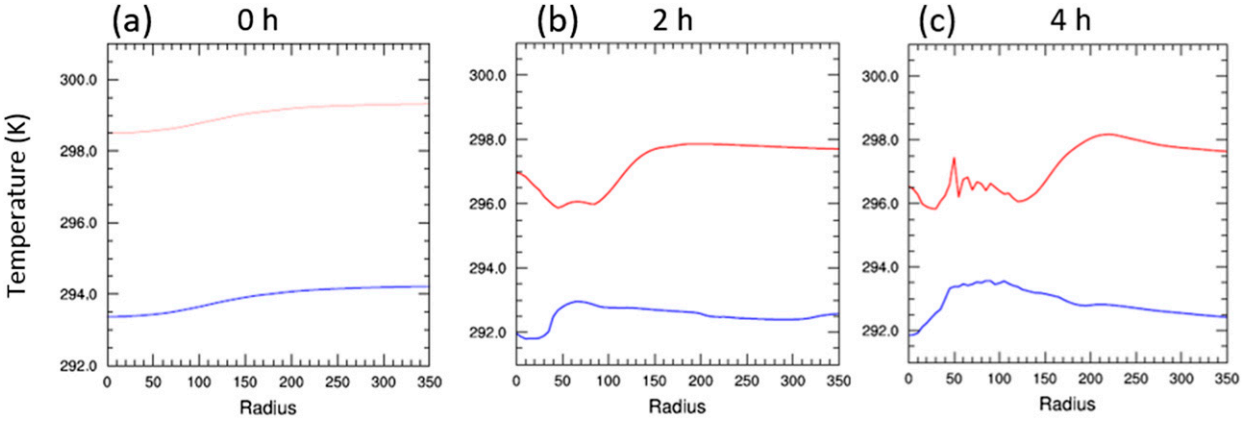

FIG. 10. Radial profile of the azimuthally averaged 950-hPa temperature (K) for C3 (blue) and W3 (red) at (a) 0, (b) 2, and (c) 4 h.

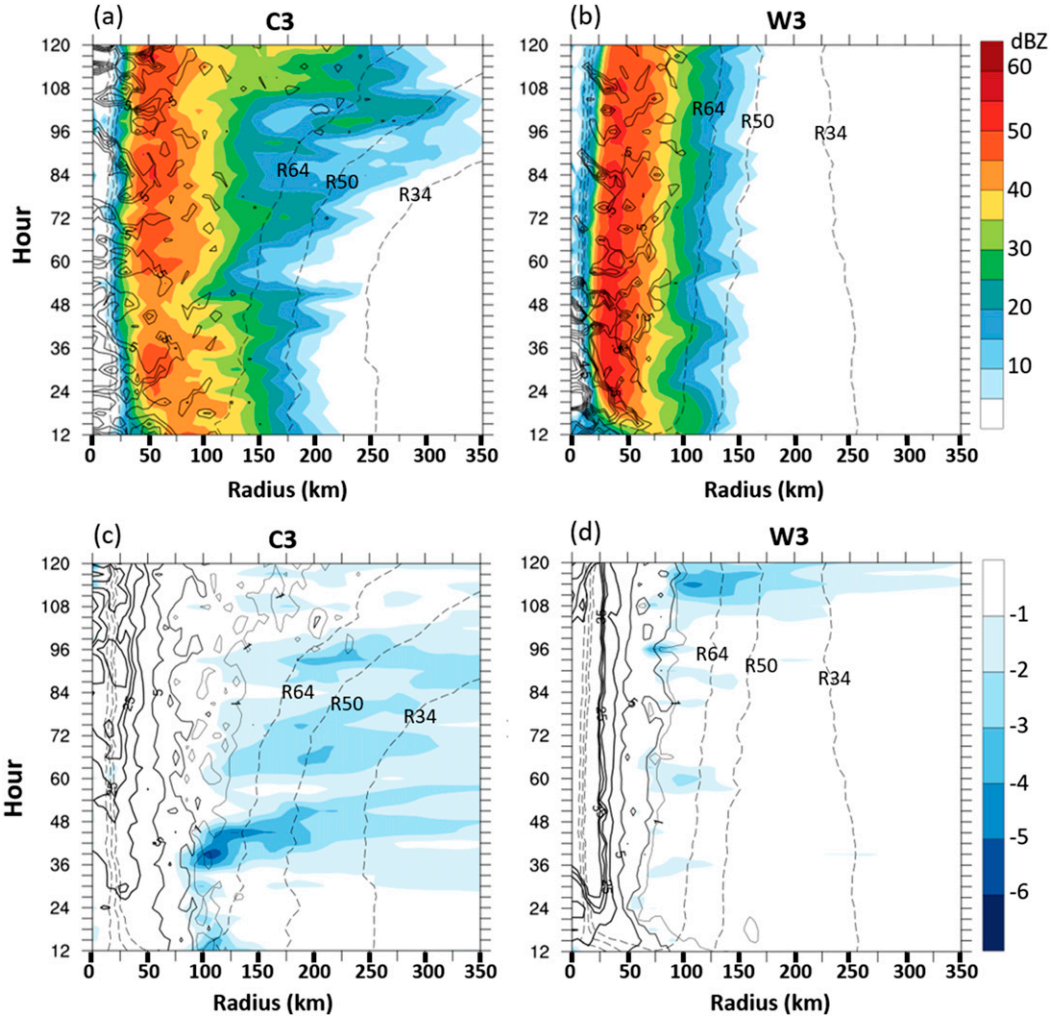

FIG. 11. Hovmöller diagrams for (left) C3 and (right) W3 of the R34, R50, and R64 tangential winds (black dashed) overlaid on PV diagnostics showing azimuthally averaged (a),(b) radar reflectivity (color shaded) and 850–400-hPa average PV tendency (black solid) and (c),(d) 850-hPa radial wind velocities (color shaded) and 850-hPa PV (black solid). The PV tendency is contoured in increments of 1 PVU $(3\,\mathrm{h})^{-1}$ from 0.5 to 4.5 PVU $(3\,\mathrm{h})^{-1}$ (1 PVU $= 10^{-6}\,\mathrm{K\,kg^{-1}\,m^2\,s^{-1}}$). Contour increments for the PV are 1, 2, 5, 15, 25, and 35 PVU.

circulation in the boundary layer to increase RAM fluxes (Li et al. 2014; Didlake and Houze 2013; Fudeyasu and Wang 2011). They also found that more active rainbands in the rapid filamentation zone were associated with enhanced flux convergence in the lower troposphere, not unlike what is observed here. Figure 6a demonstrates that, although peak rain rates are higher in W3, convection is more active beyond C3's RMW, which corresponds to the enhanced RAM fluxes above the boundary layer between 75 and 100 km from C3's center (Fig. 12a). The RAM flux convergence in the lower troposphere continually increases throughout the simulation, corresponding to the outer-core rainband activity in C3 (Figs. 12c,e).

It is likely that diabatic-PV processes in the rainbands enhance RAM fluxes above the boundary layer, but a full piecewise analysis of the inverted-PV field is needed to determine the exact contribution of diabatically generated PV to the RAM field. While this involved process is left for future work, the current results suggest that RAM flux convergence *within the boundary layer* is where the majority of gains to the overall RAM field occur. Development of rainbands beyond the RMW are then necessary to expand boundary layer inflow and increase the inward transport of RAM, leading to wind field expansion. Averaging the mean RAM flux convergence over a 60–120-h period further demonstrates that, relative to the boundary layer, the fluxes in the lower and midtroposphere are very weak (Fig. 13). Furthermore, values of at least $150\,\mathrm{m^2\,s^{-2}}$ extend beyond 600 km in C3 (Fig. 13a), while staying confined to

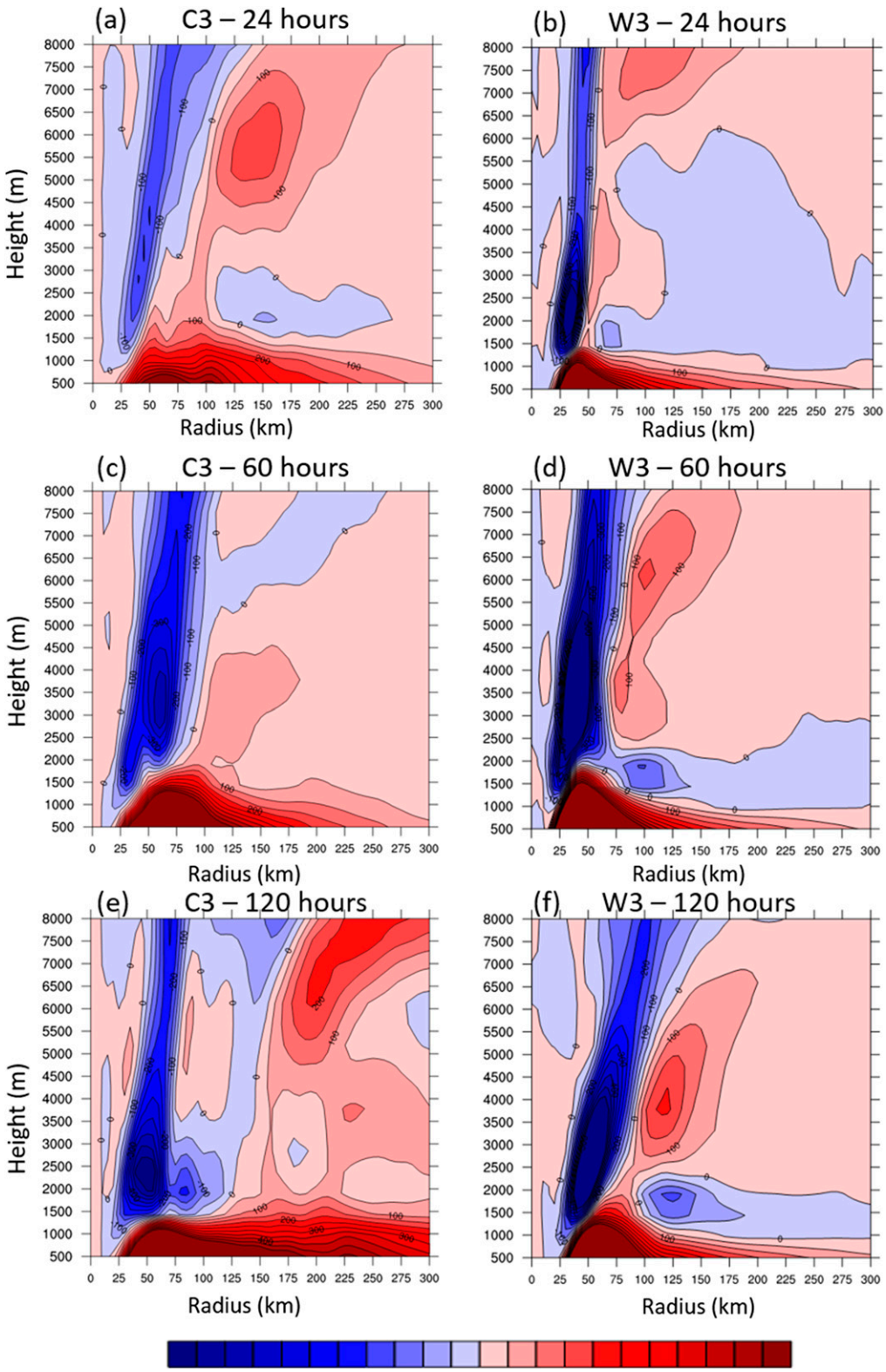

FIG. 12. Horizontal convergence of mean fluxes of RAM (color contour increment = 50 $m^2 s^{-2}$) for (left) C3 and (right) W3 at (a),(b) 24; (c),(d) 60; and (e),(f) 120 h. Positive values indicate gains to the AAM budget.

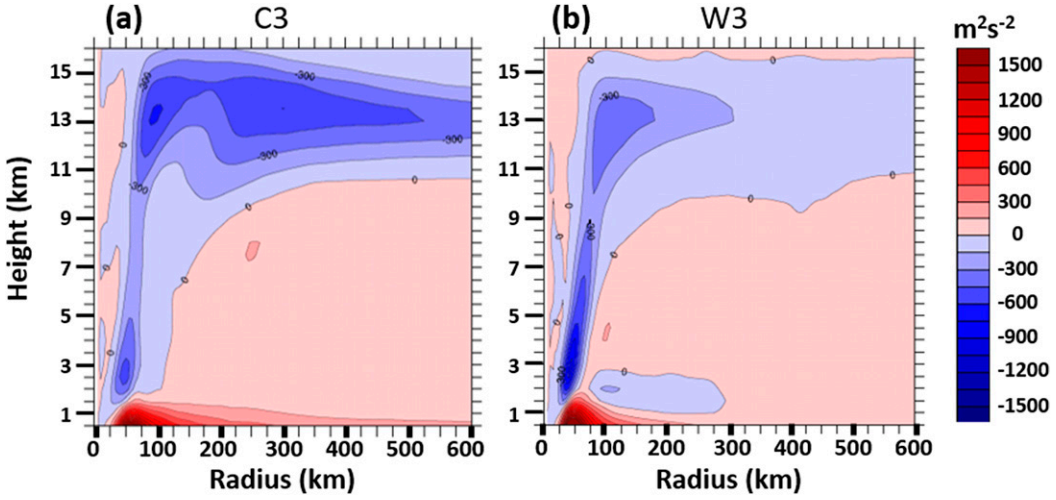

FIG. 13. Horizontal convergence of mean fluxes of RAM (contour increment = 300 $m^2 s^{-2}$) averaged over a 60–120-h period for (a) C3 and (b) W3.

250 km in W3 (Fig. 13b), explaining the final sizes of their respective R34 (i.e., Fig. 4d).

When the eddy and mean flux convergence and Coriolis torque are vertically integrated from the surface to 8 km and compared with the frictional dissipation, it becomes clearer why C3 expanded after 60 h while W3 did not. At 24 h, gains to the RAM budget outside the RMW exceed negative contributions from the frictional dissipation and negative RAM flux at the RMW for both W3 (Fig. 14a) and C3 (Fig. 14b), leading to intensification and outer-core expansion (e.g., Figs. 4a,c). Beyond a 150-km radius, the RAM fluxes in C3 exceed the values in W3 to enhance growth of the R64 in C3 at 24 h and through the end of the simulation period. Note that, at 60 h, the negative contributions from the mean fluxes and frictional dissipation at the RMW of W3 exceed positive contributions just outside of the RMW (Fig. 14c), consistent with the weakening of W3. W3 slowly weakens throughout the end of the simulation because of the small increase in friction and negative RAM fluxes at the RMW (Fig. 14e). Positive flux convergence approximately balances the negative impacts from surface friction beyond 300 km at 120 h in W3 to hinder wind field expansion. In contrast, the RAM fluxes in C3 continuously outweigh frictional effects just outside the RMW and out to a 600-km radius (Figs. 14d,f), further explaining why C3 is intensifying and expanding in the R64 and R34 wind fields.

4. Discussion

Several studies have indicated that outer spiral rainbands are a potentially important source of PV and momentum that could affect TC intensity and size changes (HL09; May and Holland 1999; Hence and Houze 2008). Our simulations show similar results, indicating a relationship between outer-core rainband formation and an expanding outer-core wind field (R64 and R50). However, the largest gains to the RAM budget occur in the boundary layer, and positive gains above the boundary layer are near zero beyond a 300-km radius. This suggests that rainband development beyond the eyewall is more important for driving strong inflow to increase fluxes of RAM in the boundary layer, and any RAM generated from diabatic PV processes is secondary to wind field expansion, especially in the R34. This is consistent with Holland and Merrill (1984), who hypothesized that much larger imports of RAM in the boundary layer are required for outer-core and overall size changes. Our results indicating the importance of boundary layer fluxes of RAM are also consistent with XW10a, XW10b, and Chan and Chan (2014).

In this set of simulations, cooling the environment relative to a control profile decreases the initial amount of CAPE and specific humidity but increases the surface energy fluxes, which are the key to the larger developing precipitation fields. During the spinup period, C3 forms a larger convective field because the boundary layer radial inflow is stronger and more expansive than in W3. The early differences in the surface radial wind field are likely a consequence of the different boundary layer mass field gradients forced by the surface fluxes. The initially low CAPE environment of C3 does little to hinder spinup and expansion of the TC wind and precipitation fields, which corresponds well with the WISHE theory that the initial amount of CAPE in the atmosphere is not a necessary component for TC development (Emanuel 1986). However, as the CAPE

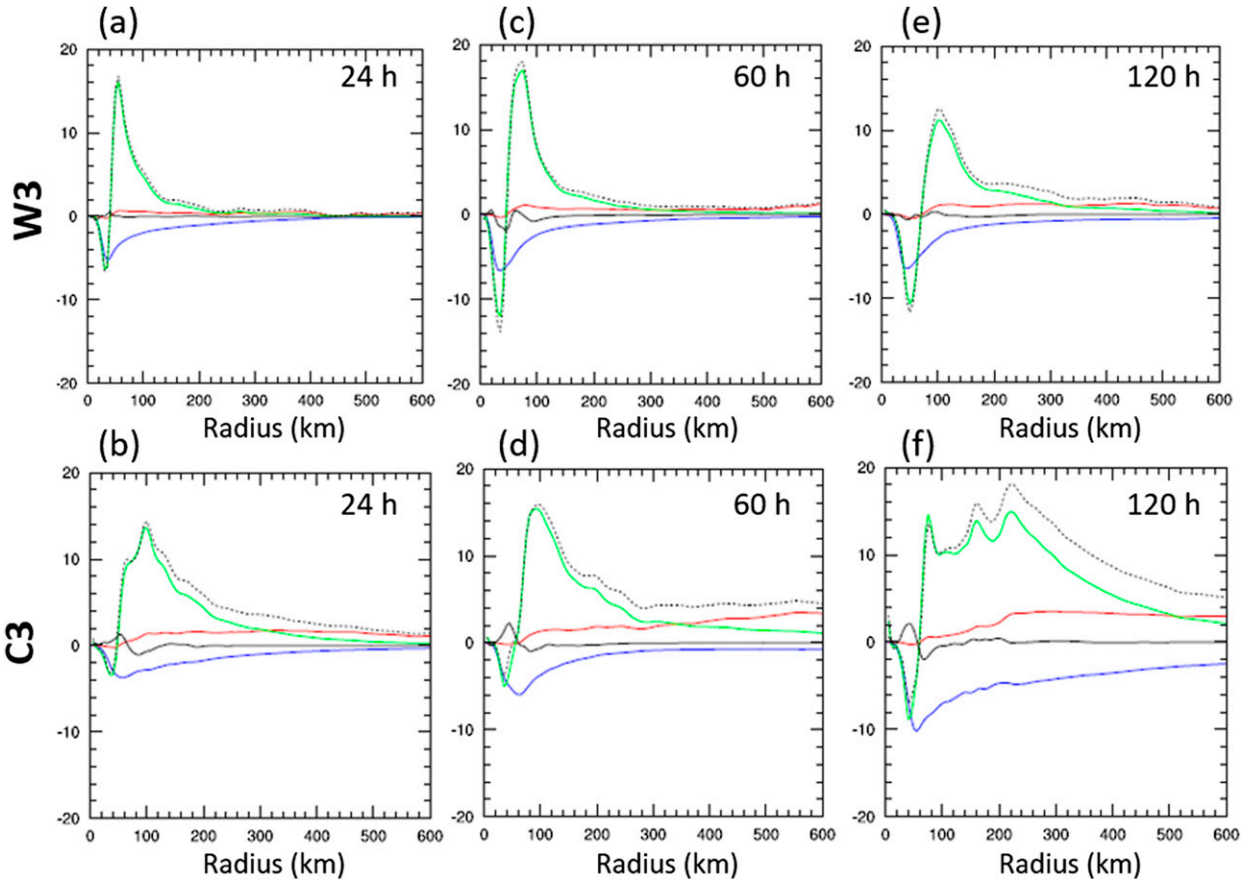

FIG. 14. Vertically integrated quantities of the RAM flux convergence ($\times 10^4$ kg s^{-2}) from the mean (green) and eddy (black) terms, symmetric Coriolis torque (red), and frictional dissipation (blue) for the (top) W3 and (bottom) C3 simulations at (a),(b) 24; (c),(d) 60; and (e),(f) 120 h. The black dashed contour is the result of adding the mean, eddy, and Coriolis terms together.

increases in C3 from the high surface fluxes, conditions become increasingly favorable for outer-rainband development, and the convective field expands. In contrast, W3 initializes with much higher CAPE, but the confined radial inflow (and thus radial convergence) limits the horizontal extent that convection can form.

After the first few hours of spinup, C3 continues to expand but begins to intensify more slowly than W3 with lower inner-core precipitation rates. Sawada and Iwasaki (2010) found that slower TC development occurs in experiments with more evaporative cooling. Evaporative cooling induces cool downdrafts and decreases CAPE near the eyewall, which is unfavorable for the development of an axisymmetric TC structure. The C3 environment is cooler and less moist than W3 when it initializes, so it is likely that evaporative cooling in the convective downdrafts is enhanced during the TC's development stage. However, outer-core rainbands are also an important source of diabatic heating outside the eyewall, which Wang (2009) suggests is important for decreasing the pressure gradient across the inner core and expanding the tangential wind field. Increased outer-core rainband activity in C3 is associated with a larger RMW throughout the majority of the simulation and is consistent with the results found in Wang (2009).

After the secondary circulation develops, the expanding convective field in C3 allows the outer core to strengthen and expand. As this occurs, RAM in the boundary layer increases outside of the outer core from increasing tangential winds at large radii. In conjunction with the expanding boundary layer radial inflow, fluxes of RAM from the environment continue to aid in the expansion of the outer core and overall wind fields. More thoroughly explained in XW10a and XW10b, this process continues in a positive feedback between enhanced fluxes and expansion of the outer-core wind field. This positive feedback is also noted in HL09. As the positive feedback between the wind field and fluxes enhances RAM, moisture, and heat at large radii, the radial inflow that also expands to large radii continues to import these quantities into the TC. A rapid expansion occurs in C3's R34 wind field after 60 h, in accordance

with increasing flux convergence of RAM in the boundary layer. We observed a small amount of RAM being generated at large radii in the W3 simulation. However, the radial inflow is so weak that the RAM imports from the environment are negligible, leading to reduced RAM flux convergence and a slight contraction in the R34. These results are consistent with those of Chan and Chan (2014) and others who suggest that lower-tropospheric forcing is responsible for TC size changes.

5. Conclusions

In this study, a set of seven idealized TC simulations is described in which a control virtual temperature profile is modified by ±1°, ±2°, and ±3°C without changing the initial relative humidity profile or the constant SST of 302 K, resulting in corresponding changes in the initial CAPE, surface energy fluxes, and specific humidity profile. Each simulation is then examined for structural changes relative to the development of the control simulation for a period of 120 h, and then the physical mechanisms for those changes are investigated. Particular focus is paid to the extremes in the set, which allows us to clearly identify the dominant factors influencing the size and intensity when the atmospheric temperature is modified.

The results indicate that the initially high CAPE and specific humidity environment of the warmest environment simulations (e.g., W3) is important for the rapid development of a very compact and more intense inner-core precipitation and wind field. In contrast, the coldest environment, C3, initializes with low CAPE and specific humidity but immediately develops a larger wind field and broader inner and outer core of convection. This suggests that high amounts of CAPE and moisture within the TC and near environment are not sufficient initial conditions for outer-core rainband development and wind field expansion.

An analysis of the early development of the radial wind circulation reveals that C3 develops a stronger and more expansive area of boundary layer radial inflow compared to W3, which allows vertical motion to develop farther from the TC center. The surface heat fluxes immediately set up a radial temperature gradient conducive to an expanded region of radial acceleration. Kepert (2012) notes that the boundary layer dynamics of simulated TCs is intricately tied to the boundary layer schemes used in the simulation. A detailed analysis of the boundary layer AAM and PV budgets to identify the trigger for rainband formation is the next logical step to identify the role of heat fluxes on radial wind structure. The primary takeaway from this study is that, even if a TC has high CAPE outside the inner core, it will not be realized as convection in rainbands unless a lifting mechanism exists in the boundary layer. In this case, radial wind convergence exists in the outer core of C3 that is much weaker in W3.

After the secondary circulation is established, high surface fluxes in C3 increase CAPE to fuel inner- and outer-core convection, which allows both the radial and tangential wind field to continue to expand. Similar to the processes observed in HL09, XW10a, and XW10b, a positive-feedback loop occurs, in which the expanding wind field increases surface fluxes and subsequent CAPE in the outer core, which enhances outer-core convection, strengthens and expands the tangential wind field, and further intensifies outer-core fluxes. In the case of C3, surface radial inflow expands with the strengthening outer-core convection that eventually becomes important for importing large quantities of RAM from the environment. In contrast, RAM imports are much lower in the W3 environment, especially at large radii, so the wind field remains relatively compact.

Several conclusions can be drawn from these simulations.

1) When the atmospheric temperature is modified without changing the SST, it is the corresponding changes in the surface fluxes that drive the size evolution of the TC.
2) Regardless of the initial amount of CAPE in the TC region, it is the extent and strength of the radial inflow outside of the RMW that drives a larger convective field during development.
3) The development of outer rainbands is key to developing a more extensive wind field. In these simulations, the development of outer rainbands is tied to the development of a more radially extensive boundary layer radial wind field with local maxima that are tied to updrafts.
4) The RAM generated from processes related to diabatic PV production in the rainbands may enhance outer-core expansion (R64 and R50) as the TC develops, but increases to the RAM and corresponding tangential wind fields are primarily linked to boundary layer processes. Flux convergence of RAM beyond the outer-core region is particularly important for overall size (R34) changes in a mature TC.

Future work includes examining the effects of the initial sizes of TCs on their ultimate size within specific environments and examining in more detail the role of the boundary layer in the development of outer rainbands.

Acknowledgments. This study is from part of the first author's Ph.D. work at The University of Arizona, which was supported by the National Science Founda-

tion Physical and Dynamic Meteorology Program under Grant AGS-0822660. The authors appreciate the constructive comments of the anonymous reviewers, which led to the improvement of this manuscript. The WRF ARW model was made available through the National Center for Atmospheric Research (NCAR). Data analysis and visualizations were performed using the NCAR Command Language (Version 6.0.0). A special thanks goes to Dr. Kimberly Wood and the Ph.D. committee members—Dr. Xubin Zeng, Dr. Yolande Serra, Dr. Katie Hirschboeck, and Dr. Dave Moore—who provided invaluable insight on the research in this manuscript.

REFERENCES

Beven, J. L., and Coauthors, 2008: Atlantic hurricane season of 2005. *Mon. Wea. Rev.*, **136**, 1109–1173, doi:10.1175/2007MWR2074.1.

Black, P. G., and R. A. Anthes, 1971: On the asymmetric structure of the tropical cyclone outflow layer. *J. Atmos. Sci.*, **28**, 1348–1366, doi:10.1175/1520-0469(1971)028<1348:OTASOT>2.0.CO;2.

Blake, E. S., C. W. Landsea, and E. J. Gibney, 2011: The deadliest, costliest, and most intense United States tropical cyclones from 1851 to 2010 (and other frequently requested hurricane facts). NOAA Tech. Memo. NWS NHC-6, 49 pp. [Available online at http://www.nhc.noaa.gov/pdf/nws-nhc-6.pdf.]

Brand, S., 1972: Very large and very small typhoons of the western North Pacific Ocean. *J. Meteor. Soc. Japan*, **50**, 332–341.

Cecil, D. J., E. J. Zipser, and S. W. Nesbitt, 2002: Reflectivity, ice scattering, and lightning characteristics of hurricane eyewalls and rainbands. Part I: Quantitative description. *Mon. Wea. Rev.*, **130**, 769–784, doi:10.1175/1520-0493(2002)130<0769:RISALC>2.0.CO;2.

Challa, M., and R. L. Pfeffer, 1980: Effects of eddy fluxes of angular momentum on model hurricane development. *J. Atmos. Sci.*, **37**, 1603–1618, doi:10.1175/1520-0469(1980)037<1603:EOEFOA>2.0.CO;2.

Chan, J. C. L., and R. T. Williams, 1987: Analytical and numerical studies of the beta effect in tropical cyclone motion. Part I: Zero mean flow. *J. Atmos. Sci.*, **44**, 1257–1265, doi:10.1175/1520-0469(1987)044<1257:AANSOT>2.0.CO;2.

Chan, K. T. F., and J. C. L. Chan, 2014: Impacts of initial vortex size and planetary vorticity on tropical cyclone size. *Quart. J. Roy. Meteor. Soc.*, **140**, 2235–2248, doi:10.1002/qj.2292.

Chavas, D. R., and K. A. Emanuel, 2010: A QuickSCAT climatology of tropical cyclone size. *Geophys. Res. Lett.*, **37**, L18816, doi:10.1029/2010GL044558.

Demuth, J., M. DeMaria, and J. A. Knaff, 2006: Improvement of advanced microwave sounder unit tropical cyclone intensity and size estimation algorithms. *J. Appl. Meteor. Climatol.*, **45**, 1573–1581, doi:10.1175/JAM2429.1.

Didlake, A. C., and R. A. Houze, 2013: Convective-scale variations in the inner-core rainbands of a tropical cyclone. *J. Atmos. Sci.*, **70**, 504–523, doi:10.1175/JAS-D-12-0134.1.

Dudhia, J., 1989: Numerical study of convection observed during the winter monsoon experiment using a mesoscale two-dimensional model. *J. Atmos. Sci.*, **46**, 3077–3107, doi:10.1175/1520-0469(1989)046<3077:NSOCOD>2.0.CO;2.

Emanuel, K. A., 1986: An air–sea interaction theory for tropical cyclones. Part I: Steady-state maintenance. *J. Atmos. Sci.*, **43**, 585–605, doi:10.1175/1520-0469(1986)043<0585:AASITF>2.0.CO;2.

Fang, J., and F. Zhang, 2012: Effect of beta shear on simulated tropical cyclones. *Mon. Wea. Rev.*, **140**, 3327–3346, doi:10.1175/MWR-D-10-05021.1.

Frank, W. M., and E. A. Ritchie, 1999: Effects of environmental flow upon tropical cyclone structure. *Mon. Wea. Rev.*, **127**, 2044–2061, doi:10.1175/1520-0493(1999)127<2044:EOEFUT>2.0.CO;2.

——, and ——, 2001: Effects of vertical wind shear on the intensity and structure of numerically simulated hurricanes. *Mon. Wea. Rev.*, **129**, 2249–2269, doi:10.1175/1520-0493(2001)129<2249:EOVWSO>2.0.CO;2.

Fudeyasu, H., and Y. Wang, 2011: Balanced contribution to the intensification of a tropical cyclone simulated in TCM4: Outer-core spinup process. *J. Atmos. Sci.*, **68**, 430–449, doi:10.1175/2010JAS3523.1.

Hence, D. A., and R. A. Houze, 2008: Kinematic structure of convective-scale elements in the rainbands of Hurricanes Katrina and Rita (2005). *J. Geophys. Res.*, **113**, D15108, doi:10.1029/2007JD009429.

Hill, K. A., and G. M. Lackmann, 2009: Influence of environmental humidity on tropical cyclone size. *Mon. Wea. Rev.*, **137**, 3294–3315, doi:10.1175/2009MWR2679.1.

Holland, G. J., 1983: Angular momentum transports in tropical cyclones. *Quart. J. Roy. Meteor. Soc.*, **109**, 187–209, doi:10.1002/qj.49710945909.

——, and R. T. Merrill, 1984: On the dynamics of tropical cyclone structure changes. *Quart. J. Roy. Meteor. Soc.*, **110**, 723–745, doi:10.1002/qj.49711046510.

Hong, S.-Y., and J.-O. J. Lim, 2006: The WRF single-moment 6-class microphysics scheme (WSM6). *J. Korean Meteor. Soc.*, **42**, 129–151.

Irish, J. L., D. T. Resio, and J. J. Ratcliff, 2008: The influence of storm size on hurricane surge. *J. Phys. Oceanogr.*, **38**, 2003–2013, doi:10.1175/2008JPO3727.1.

Janjic, Z. I., 1990: The step-mountain coordinate: Physical package. *Mon. Wea. Rev.*, **118**, 1429–1443, doi:10.1175/1520-0493(1990)118<1429:TSMCPP>2.0.CO;2.

——, 1994: The step-mountain eta coordinate model: Further developments of the convection, viscous sublayer, and turbulence closure schemes. *Mon. Wea. Rev.*, **122**, 927–945, doi:10.1175/1520-0493(1994)122<0927:TSMECM>2.0.CO;2.

——, 2002: Nonsingular implementation of the Mellor–Yamada level 2.5 scheme in the NCEP Meso model. NCEP Office Note 437, 61 pp.

Kain, J. S., and J. M. Fritsch, 1993: Convective parameterization for mesoscale models: The Kain–Fritcsh scheme. *The Representation of Cumulus Convection in Numerical Models, Meteor. Monogr.*, No. 46, Amer. Meteor. Soc., 246 pp., doi:10.1007/978-1-935704-13-3_16.

Kepert, J. D., 2012: Choosing a boundary layer parameterization for tropical cyclone modeling. *Mon. Wea. Rev.*, **140**, 1427–1445, doi:10.1175/MWR-D-11-00217.1.

Kimball, S. K., 2006: A modeling study of hurricane landfall in a dry environment. *Mon. Wea. Rev.*, **134**, 1901–1918, doi:10.1175/MWR3155.1.

——, and M. S. Mulekar, 2004: A 15-year climatology of North Atlantic tropical cyclones. Part I: Size parameters. *J. Climate*, **17**, 3555–3575, doi:10.1175/1520-0442(2004)017<3555:AYCONA>2.0.CO;2.

Knaff, S. K., S. P. Longmore, and D. A. Molenari, 2014: An objective satellite-based tropical cyclone size climatology. *J. Climate*, **27**, 455–476, doi:10.1175/JCLI-D-13-00096.1.

Li, Q., Y. Wang, and Y. Duan, 2014: Effects of diabatic heating and cooling in the rapid filamentation zone on structure and

intensity of a simulated tropical cyclone. *J. Atmos. Sci.*, **71**, 3144–3163, doi:10.1175/JAS-D-13-0312.1.

——, ——, and ——, 2015: Impacts of evaporation of rainwater on tropical cyclone structure and intensity—A revisit. *J. Atmos. Sci.*, **72**, 1323–1345, doi:10.1175/JAS-D-14-0224.1.

Ma, Z., J. Fei, X. Huang, and X. Cheng, 2015: Contributions of surface sensible heat fluxes to tropical cyclone. Part I: Evolution of tropical cyclone intensity and structure. *J. Atmos. Sci.*, **72**, 120–140, doi:10.1175/JAS-D-14-0199.1.

Maclay, K. S., M. DeMaria, and T. H. Vonder Haar, 2008: Tropical cyclone inner-core kinetic energy evolution. *Mon. Wea. Rev.*, **136**, 4882–4898, doi:10.1175/2008MWR2268.1.

Malkus, J. S., and H. Riehl, 1960: On the dynamics and energy transformations in a steady-state hurricane. *Tellus*, **12A**, 1–20, doi:10.1111/j.2153-3490.1960.tb01279.x.

Mallard, M. S., G. M. Lackmann, A. Aiyyer, and K. Hill, 2013: Atlantic hurricanes and climate change. Part I: Experimental design and isolation of thermodynamic effects. *J. Climate*, **26**, 4876–4893, doi:10.1175/JCLI-D-12-00182.1.

May, P. T., and G. J. Holland, 1999: The role of potential vorticity generation in tropical cyclone rainbands. *J. Atmos. Sci.*, **56**, 1224–1228, doi:10.1175/1520-0469(1999)056<1224:TROPVG>2.0.CO;2.

McBride, J. L., 1981: Observational analysis of tropical cyclone formation. Part III: Budget analysis. *J. Atmos. Sci.*, **38**, 1152–1166, doi:10.1175/1520-0469(1981)038<1152:OAOTCF>2.0.CO;2.

——, and R. M. Zehr, 1981: Observational analysis of tropical cyclone formation. Part II: Comparison of non-developing vs. developing systems. *J. Atmos. Sci.*, **38**, 1132–1151, doi:10.1175/1520-0469(1981)038<1132:OAOTCF>2.0.CO;2.

Merrill, R. T., 1984: A comparison of large and small tropical cyclones. *Mon. Wea. Rev.*, **112**, 1408–1418, doi:10.1175/1520-0493(1984)112<1408:ACOLAS>2.0.CO;2.

Mlawer, E. J., S. J. Taubman, P. D. Brown, M. J. Iacono, and S. A. Clough, 1997: Radiative transfer for inhomogeneous atmosphere: RRTM, a validated correlated-k model for the longwave. *J. Geophys. Res.*, **102**, 16 663–16 682, doi:10.1029/97JD00237.

Molinari, J., P. Moore, and V. Idone, 1999: Convective structure of hurricanes as revealed by lightning locations. *Mon. Wea. Rev.*, **127**, 520–534, doi:10.1175/1520-0493(1999)127<0520:CSOHAR>2.0.CO;2.

Persing, J., and M. T. Montgomery, 2005: Is environmental CAPE important in the determination of maximum possible hurricane intensity? *J. Atmos. Sci.*, **62**, 542–550, doi:10.1175/JAS-3370.1.

Ritchie, E. A., and R. L. Elsberry, 2007: Simulations of the extratropical transition of tropical cyclones: Phasing between the upper-level trough and tropical cyclone. *Mon. Wea. Rev.*, **135**, 862–876, doi:10.1175/MWR3303.1.

——, and W. M. Frank, 2007: Interactions between simulated tropical cyclones and an environment with a variable Coriolis parameter. *Mon. Wea. Rev.*, **135**, 1889–1905, doi:10.1175/MWR3359.1.

Saffir, H. S., 1973: Hurricane wind and storm surge. *Military Eng.*, **423**, 4–5.

Sawada, M., and T. Iwasaki, 2010: Impacts of evaporation from raindrops on tropical cyclones. Part I: Evolution and axisymmetric structure. *J. Atmos. Sci.*, **67**, 71–83, doi:10.1175/2009JAS3040.1.

Simpson, R. H., 1974: The hurricane disaster potential scale. *Weatherwise*, **27**, 169–186, doi:10.1080/00431672.1974.9931702.

Skamarock, W. C., J. B. Klemp, J. Dudhia, D. O. Gill, D. M. Barker, W. Wang, and J. G. Powers, 2005: A description of the Advanced Research WRF version 2. NCAR Tech. Note NCAR/TN-468+STR. 88 pp., doi:10.5065/D6DZ069T.

Tuleya, R. E., and Y. Kurihara, 1975: The energy and angular momentum budget of a three-dimensional tropical cyclone model. *J. Atmos. Sci.*, **32**, 287–301, doi:10.1175/1520-0469(1975)032<0287:TEAAMB>2.0.CO;2.

Wang, Y., 2009: How do outer spiral rainbands affect tropical cyclone structure and intensity? *J. Atmos. Sci.*, **66**, 1250–1273, doi:10.1175/2008JAS2737.1.

Weatherford, C. L., and W. M. Gray, 1988a: Typhoon structure as revealed by aircraft reconnaissance. Part I: Data analysis and climatology. *Mon. Wea. Rev.*, **116**, 1032–1043, doi:10.1175/1520-0493(1988)116<1032:TSARBA>2.0.CO;2.

——, and ——, 1988b: Typhoon structure as revealed by aircraft reconnaissance. Part II: Structural variability. *Mon. Wea. Rev.*, **116**, 1044–1056, doi:10.1175/1520-0493(1988)116<1044:TSARBA>2.0.CO;2.

Xu, J., and Y. Wang, 2010a: Sensitivity of tropical cyclone inner-core size and intensity to the radial distribution of surface entropy flux. *J. Atmos. Sci.*, **67**, 1831–1852, doi:10.1175/2010JAS3387.1.

——, and ——, 2010b: Sensitivity of the simulated tropical cyclone inner-core size to the initial vortex size. *Mon. Wea. Rev.*, **138**, 4135–4157, doi:10.1175/2010MWR3335.1.